Nonlinear defects separating spiral waves in Taylor-Couette flow

Ch. Hoffmann,[1,*] M. Heise,[2,†] S. Altmeyer,[1] J. Abshagen,[2] A. Pinter,[1] G. Pfister,[2] and M. Lücke[1]
[1]*Institut für Theoretische Physik, Universität des Saarlandes, D-66123 Saarbrücken, Germany*
[2]*Institut für Experimentelle und Angewandte Physik, Universität Kiel, D-24098 Kiel, Germany*
(Received 6 September 2009; published 11 December 2009)

Stable domain walls which are realized by a defect between oppositely traveling spiral waves in a pattern-forming hydrodynamic system, i.e., Taylor-Couette flow, are studied numerically as well as experimentally. A nonlinear mode coupling resulting from the nonlinearities in the underlying momentum balance is found to be essential for the stability of the defects. These nonlinearly driven defects separate spiral domains and act either as a phase generating or annihilating defect. Specific phase differences of either 0 or π between the participating traveling waves are a characteristic feature of this defect. The influence of a symmetry breaking externally imposed flow on the spiral domains and the defects is studied. The numerical and experimental results are in excellent agreement.

DOI: 10.1103/PhysRevE.80.066308 PACS number(s): 47.20.Ky, 05.45.−a, 02.30.Oz

I. INTRODUCTION

Structured states appear spontaneously as a result of a pattern-forming instability in a large variety of driven nonequilibrium systems, e.g., in optics, chemical and biological models, polymer and binary mixtures, liquid crystals, convection, and shear flow [1–3]. However, also patches, i.e., spatial domains with different order parameters or symmetries of the structures, exist in these systems. The formation of such domains and their interaction via domain walls which are realized via defects has often been investigated close to onset.

Simple examples are one-dimensional (1D) patterns of oppositely traveling waves (TW) [3–6] that appear, e.g., via a forward Hopf bifurcation in systems with spatial translation and reflection symmetry. Also the defects between two such TW, i.e., their sources or sinks are close to onset described by coupled Ginzburg-Landau equations for slowly varying amplitudes of the two critical TW modes [7,8]—see, however, the deviations at larger distance from threshold in [4]. On the other hand, two-dimensional (2D) patterns allow defects and domains with more complex spatiotemporal behavior. However, coupled Ginzburg-Landau equations or order-parameter equations that are based on the critical modes of the pattern in question have been used successfully also for these systems to model various aspects of their behavior [1–3,9–12].

One of the classical systems for the study of bifurcation events and nonlinear pattern formation is the Taylor-Couette system, i.e., the flow of a viscous fluid in the gap between two concentric and independently rotating cylinders [13,14]. It is one of the best controllable hydrodynamic systems and allows quantitative comparisons between experiments and numerical simulations of the Navier-Stokes equations even beyond the first instability. In the axial periodic or infinite Taylor-Couette system, upwards and downwards traveling spirals (SPI) appear via a symmetry breaking Hopf bifurcation out of the circular Couette flow (CCF).

On the other hand, finite systems—e.g., in experimental setups—are typically confined by nonrotating rigid end walls, thus, the translational invariance is broken. These end walls at top and bottom subcritically drive axisymmetric Ekman vortices in the annulus. As a consequence, spiral vortices only exist in a bulk region bounded by "wavylike" rotating defects in the vicinity of the axisymmetric Ekman vortices near the ends. These Ekman-spiral defects can be classified into two types: phase generating and annihilating defects. Thus, spirals in finite systems differ in their spatiotemporal properties from those spirals in infinite systems [15,16]. However, in the finite case, the transition to upwards and downwards traveling spirals has also been understood as Hopf bifurcation [17–19].

In a recent letter [20], we pointed out the existence of nonlinear defects between two axially separated domains of spiral waves traveling into opposite directions. So far, we investigated phase generating spiral-spiral defects which are stabilized by a strongly nonlinear balance of generalized forces.

Here, a more comprehensive study (in the finite and the axial periodic system) of phase generating and, in particular, annihilating spiral-spiral defects as well as the analysis of the amplitudes and the phase differences between the participating traveling spirals is performed using experimental and numerical methods. Further, we investigate the stability of states consisting of domains of different (axially localized) spiral waves separated by spiral-spiral defects.

II. SYSTEM

The system consists of two concentric, independently rotating cylinders (inner, outer radius $r_{1,2}$ angular velocities $\Omega_{1,2}$) with a fluid of kinematic viscosity ν in the gap between them. Lengths are scaled by the gap width $d=r_2-r_1$, time by the diffusion time $\tau=d^2/\nu$ and the velocities by d/τ. Control parameters are the inner and outer cylinder Reynolds numbers,

$$R_1 = r_1\Omega_1 d/\nu, \quad R_2 = r_2\Omega_2 d/\nu, \tag{1}$$

and the Reynolds number Re of the externally imposed axial through flow given by the mean axial velocity $\langle w\rangle_{r,\varphi}$ aver-

*chhof@lusi.uni-sb.de
†heise@physik.uni-kiel.de

 ©2009 The American Physical Society

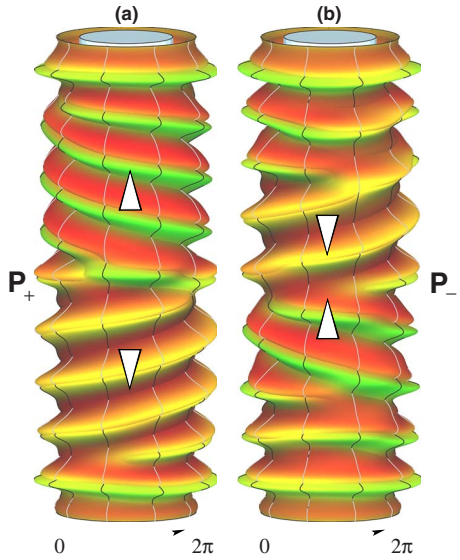

FIG. 1. (Color online) Three-dimensional (3D) visualization of $u(\varphi,z)$ at midgap (for better visibility, the whole 2π cylinder is displayed). The flow in (a) contains a phase generating defect (P_+) at midheight, the flow in (b) a phase annihilating defect (P_-). In each case the phase difference at the defect location is $\alpha=\pi$ (see below). Phase propagation is indicated by white arrows. Parameters are $\eta=0.5$, $\Gamma=12$, $R_1=118$, and $R_2=-100$.

aged over the annular cross section. Geometric parameters are the aspect ratio $\Gamma=L/d$ and the radius ratio $\eta=r_1/r_2$. Throughout this article, the radius ratio $\eta=0.5$, the aspect ratio $\Gamma=16$ (for the case of a finite system), and $R_2=-125$ (except for Fig. 1) are held constant.

A. Numerical method

The flow is governed by the Navier-Stokes equations (NSEs) for incompressible fluids ($\nabla\cdot\mathbf{u}=0$),

$$\partial_t\mathbf{u}=\nabla^2\mathbf{u}-(\mathbf{u}\cdot\nabla)\cdot\mathbf{u}-\nabla p. \tag{2}$$

Using cylindrical coordinates, we decompose the velocity field $\mathbf{u}=u\mathbf{e}_r+v\mathbf{e}_\varphi+w\mathbf{e}_z$ into a radial component u, an azimuthal one v, and an axial one w. For numerical calculations, we used the G1D3 code, a combination of a Galerkin method in azimuthal direction (Eq. (3)) and finite differences in axial and radial direction as well as in time. We used homogeneous grids with discretization lengths $\Delta r=\Delta z=0.05$ for the four fields u, v, w, and the pressure p which are arranged on staggered grids so that they do not fall together with discontinuities in the corners. In azimuthal direction eight Fourier modes are used. See [15] for more details. At the axial ends, rigid boundary conditions were imposed in order to simulate nonrotating lids.

The velocity fields are decomposed into azimuthal Fourier modes (m) as

$$f(r,\varphi,z)=\sum_m f_m(r,z)e^{i(m\varphi)},\quad f\in\{u,v,w,p\}. \tag{3}$$

For diagnostic of the numerically/experimentally obtained fields, we also considered an additional axial Fourier mode (n) decomposition

$$f(r,\varphi,z)=\sum_{m,n} f_{m,n}(r)e^{i(m\varphi+nkz)},\quad f\in\{u,v,w,p\}. \tag{4}$$

The mode amplitudes $|u_m|$ and $|u_{m,n}|$ at midgap are used as order parameters in the following.

B. Experimental setup

In our experiments the temperature of the fluid is thermostatically controlled to (24.00 ± 0.01) °C. Silicone oil with a kinematic viscosity $\nu=10.6$ cS is used as working fluid. The inner cylinder of the apparatus is machined from stainless steel having a radius of $r_1=(12.50\pm0.01)$ mm, while the outer cylinder is made from optically polished glass with a radius of $r_2=(25.00\pm0.01)$ mm. At top and at bottom, the fluid is confined by massive end walls and the tilt of each wall is better that 0.03 mm at the outer diameter. For the case of an additional axial through flow the massive walls are systematically perforated in order to enable mass flow in axial direction. Size and distribution of the small holes in the end wall are carefully chosen in order to enable an inlet flow profile that is as similar as possible to axisymmetric Poiseuille flow. The end walls are designed in a way to avoid the azimuthal velocity component of the axial through flow at the inlet.

We utilize laser Doppler velocimetry (LDV) for measurements of the local radial and axial velocity of the flow. In this work, two different LDV measurement techniques are used. The first method measures the velocity component u or w at a fixed position (r,φ,z). The second one is an axial scan of u or w moving the LDV with constant velocity in z at fixed r and φ. In order to study the complete spatiotemporal behavior of the flow, sequential axial scans are performed for u and w.

For flow visualization purposes, aluminum flakes with a length of 80 μm are added to the fluid. Flow visualization measurements are performed by monitoring the system with a charge-coupled device camera in front of the cylinder recording the luminosity along a narrow axial stripe. The spatiotemporal behavior of the flow is then represented by successive stripes for each time step at a constant φ position leading to continuous space time plots.

III. DEFECTS IN FINITE SYSTEMS

As discussed above, in a finite system global spiral vortices only exist in the bulk region between two rotating Ekman-spiral defects that are located in the vicinity of the nonrotating rigid end walls. Since traveling waves (spirals) transport phase either upwards (L-SPI) or downwards (R-SPI), the phase in a finite system has to be generated in one defect and annihilated in the other. Thus, an L-SPI (R-SPI) in a finite system has a phase generating (annihilating) Ekman-spiral defect at the bottom and a phase annihilating (generating) one at the top.

Furthermore, in finite systems, we observed—in experiments as well as in simulations—stable, stationary states with adjacent domains of spirals with different chirality that interact either in a phase generating or annihilating defect which are located somewhere in the bulk. These spiral-spiral

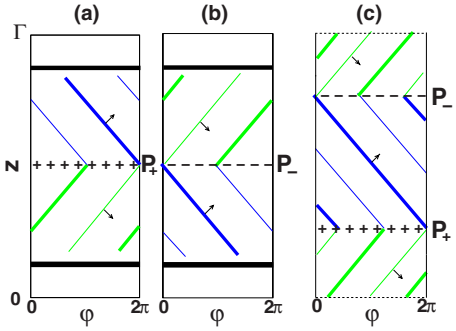

FIG. 2. (Color online) Schematic overview of three different realizations of the defect structure in the (φ,z) plane with (a) a P_+ defect, (b) a P_- defect, and (c) a combined P_+ and P_- defect, in the finite (a) and (b) and (c) the axial periodic system. All phase shifts are $\alpha=\pi$ (see below). The phase propagation is indicated by small black arrows, thick (thin) colored lines correspond to the maxima (minima) of the u field. L-SPI are indicated by blue (dark gray), R-SPI by green (light gray) color, and Ekman vortices in (a) and (b) by thick black horizontal lines.

defects differ from the Ekman-spiral defects due to the interaction of *two* spirals, L-SPI and R-SPI, instead of one spiral and the axisymmetric Ekman mode. The simplest case of a defect with two spirals—a localized L-SPI in one half of the system and a localized R-SPI in the other half—is depicted in two different realizations in Fig. 1.

The P_+ defect in the axial middle of the system in Fig. 1(a) acts as a phase (P) generating (+) defect for both spirals. The phase of each localized spiral is annihilated in the respective Ekman-spiral defect at the end walls. In (b), on the other hand, the Ekman-spiral defects generate phase which is annihilated (−) in a so-called P_- defect in the axial middle. The structure of these defect regions is stable and rotates as a whole with the same speed as the spirals. The P_+ and P_- states, as discussed so far, are schematically depicted in Figs. 2(a) and 2(b) as isolines of maximal (thick colored lines) and minimal (thin colored lines) radial velocity $u(\varphi,z)$ at midgap plotted in the (φ,z) plane of an unrolled cylinder. The type of defect is indicated by plus signs for phase generation and minus signs for phase annihilation in these plots. Note, that the phase shift α between both spirals is always π, which implies that (at the defect) the maximal u of the L-SPI coincide with the minimal u of the R-SPI and vice versa. The presence of Ekman vortices near the top and the bottom is indicated by the thick black horizontal lines.

In axial periodic systems, on the other hand, simultaneous occurrence of an L-SPI and an R-SPI domain requires *two* defects as depicted in Fig. 2(c): a phase generating P_+ and a phase annihilating P_-. The dynamics of such a configuration will be discussed later in this article.

Figure 3 depicts mode decompositions of the experimentally obtained velocity field (a) and (b) w and (c) u in the meridional plane. In the vicinity of a P_+ defect, the amplitude of the R-SPI mode (a) w_{-1} and the L-SPI mode (b) w_1 [cf. Eq. (3) for the mode decomposition] is illustrated. They overlap in the P_+ defect at $z\approx 7.5$ and each one penetrates the region of the other. Together with $u_{\pm 1}$ of both spiral modes in Fig. 3(c) which vanishes at any radial position in

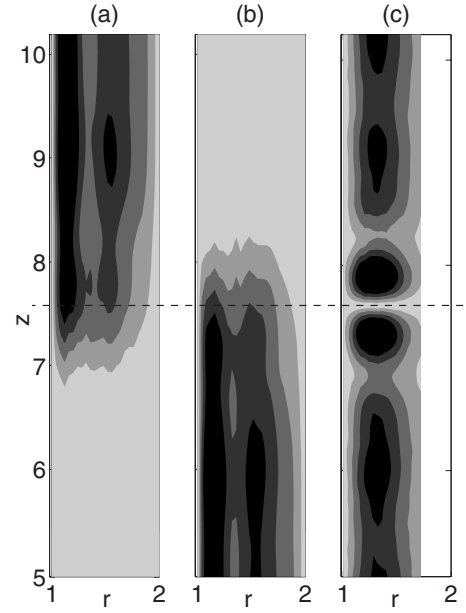

FIG. 3. Gray coded (black corresponds to the maximal value) spiral amplitudes (a) w_{+1}, (b) w_{-1}, and (c) $u_{\pm 1}$ [cf. Eq. (3) for the mode decomposition] in a meridional plane in the vicinity (cutout $5<z<10.2$) of a P_+ defect with a phase shift $\alpha=\pi$ (see below) at midheight (dashed line). White regions are experimentally inaccessible ($R_1=140$).

the defect itself, one gets a better impression of the spiral amplitudes near the defect. However, we also found the reverse type of defect where the amplitude of w vanishes and u remains finite. All defects have in common that the amplitude of exactly one velocity component, i.e., either $u_{\pm 1}$ or $w_{\pm 1}$, is zero at any radial position in the defect (cf. table below).

Besides the spiral amplitudes, also the axisymmetric mode u_0 and w_0 is found to be relevant for the stability of the P_+ or P_- defect. A vector field plot in a meridional plane of this stationary mode based on experimental and numerical data is displayed in Figs. 4(a) and 4(b). Experimental results of a $\Gamma=16$ system are presented in (a), whereas in (b), the numerical data of an axial periodic system with $\Gamma=7.2$ is displayed. The colored lines with the arrows in (a) and (b) indicate the circulation of the L-SPI in blue (dark gray) and that one caused by R-SPI in green (light gray). Near the inner cylinder, the circulation flow caused by the $m=0$ modes, $u_0\mathbf{e}_r+w_0\mathbf{e}_z$, in both systems is always axially directed to the same direction as the phase propagation of the spirals, e.g., upwards for L-SPI and downwards for R-SPI. This large circulation is additionally illustrated in Figs. 4(c)–4(e) where the axial velocity w_0 is plotted in radial direction for three different z positions, i.e., (c) above ($z=9.5$), (d) along ($z=7.8$) and (e) below the P_+ defect ($z=5.5$). These axial positions are indicated as dashed arrows in (a) and (b). The symbols (○) correspond to the experimental values of Fig. 4(a) and solid lines indicate the numerically determined values in the axial periodic system (b) of the flow.

It is clearly visible that the axial flow near the inner cylinder is directed upwards above the defect and downwards below it. This is reversed in the vicinity of the outer cylinder.

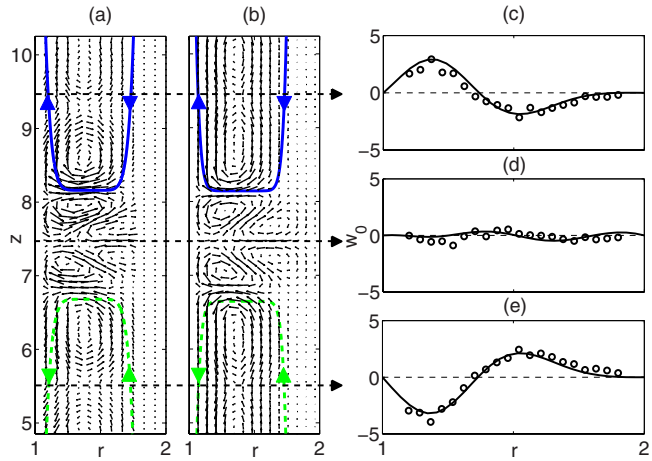

FIG. 4. (Color online) (a), (b) Vector plots (cutouts $4.9<z<10.2$ of a $\Gamma=16$ system) of flow $u_0\mathbf{e}_r+w_0\mathbf{e}_z$ generated by the axisymmetric amplitudes [cf. Eq. (3)] in the vicinity of a P_+ defect with phase shift $\alpha=\pi$. (a) Experimental measurements in a finite system and (b) numerical simulations in an axial periodic system. The colored lines with the arrows in (a) and (b) indicate the circulation of the L-SPI [solid, blue (dark gray)] and the R-SPI [dashed, green (light gray)]. Near the inner cylinder, this circulation is always axially directed in the same direction as the phase propagation of the spiral, e.g., upwards for the L-SPI and downwards for the R-SPI. The horizontal dashed arrows indicate three axial positions of the radial profiles of w_0 in (c)–(e). The symbols (○) indicate the experimental and the solid line indicates the numerically determined values ($R_1=140$).

In particular, the axial flow is zero at any radial position along the defect itself, as illustrated in Fig. 4(d). Thus, the defect behaves in some respect such as a wall.

The spirals within two adjacent spiral domains have a fixed phase relation (phase shift $\alpha=\pi$) in the defect. Figure 5 gives an overview of the four observed stable kinds of defects.

The structural properties of the corresponding phase generating or annihilating defect are shown by isosurfaces of the numerically determined azimuthal vorticity $\partial_z u-\partial_r w=\pm 60$. The diagrams on the right indicate schematically the position of the maximal (thick colored line) and the minimal (thin colored line) u of the respective spiral. They can be distinguished by their respective mode indices m and the color, i.e., L-SPI ($m=+1$) in blue (dark gray) and R-SPI ($m=-1$) in green (light gray). In Figs. 5(a) and 5(b), both defects generate phase and the spirals have a phase difference of $\alpha=\pi$, so called $P_{+,\pi}$, in (a) and $\alpha=0$, so called $P_{+,0}$, in (b). In Figs. 5(c) and 5(d), the defects annihilate phase with a phase difference of either (c) $\alpha=\pi$ or (d) $\alpha=0$, so called $P_{-,\pi}$ and $P_{-,0}$, respectively. Each of these states are found to be stable in a finite Taylor-Couette system. The following table gives the phase shifts in u as well as in the w in a $P_{+,\alpha}$ and $P_{-,\alpha}$ defect with a given α

	$P_{+,0}$	$P_{+,\pi}$	$P_{-,0}$	$P_{-,\pi}$
u	0	π	0	π
w	π	0	π	0

.

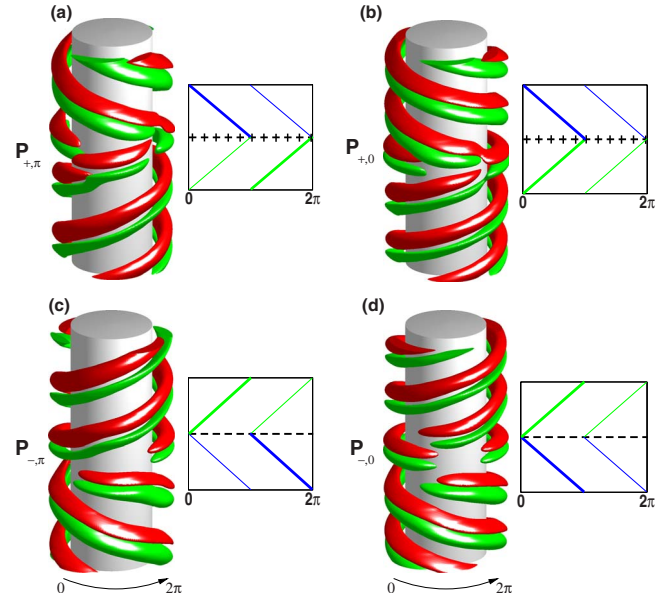

FIG. 5. (Color online) Overview of four different kinds of defects. The 3D plots show the structural properties of the defects by isosurfaces of the numerically determined azimuthal vorticity $\partial_z u-\partial_r w=\pm 60$—positive [red (dark gray)], negative [green (light gray)]. The thick (thin) solid lines in the line plots correspond to the maximal (minimal) u of the spirals: L-SPI [blue (dark gray)], R-SPI [green (light gray)]. In (a) and (b), the defects generate the phase of the spirals having a phase difference of (a) $\alpha=\pi$ and (b) $\alpha=0$. In (c) and (d) the defects are phase annihilating with the phase differences (c) $\alpha=\pi$ and (d) $\alpha=0$.

IV. DEFECTS IN AXIAL PERIODIC SYSTEMS

The general behavior of isolated P_+ and P_- defects should be studied without the influence of the boundary induced underlying Ekman vortices in an axial infinite long or periodic system. In fact, rigid lids imposing $m=0$ disturbances are not necessary for the system to generate $P_\pm$ defects. A sufficiently long system $\Gamma\gtrsim 12$ with periodic boundary conditions allows a state consisting of a phase generating P_+ and a phase annihilating P_- defect which separate R-SPI and L-SPI domains as schematically illustrated in Fig. 2(c). Such a state can be prepared numerically by mirroring extended spirals. Furthermore, by imposing glide-mirror transformations, arbitrary phase shifts α of the $m=\pm 1$ modes in the defect are also obtainable as initial conditions.

Simulations showed that the periodic system prefers $P_{\pm,\alpha}$ with $\alpha=\pi$, i.e., other phase shifts $\alpha\neq\pi$ are unstable and disappear when chosen as initial state for the benefit of a $P_{\pm,\pi}$. In the *finite* system with rigid end walls, we found stable states with $\alpha=\pi$ and additionally $\alpha=0$ which is a significant difference between both types of boundary conditions. However, for a given periodicity length Γ, the flow has to enlarge or shrink the localized spiral domains in order to obtain the preferred phase shift. We found that the shrinking (expansion) of a region is accompanied by a decrease (increase) of the spiral amplitudes in the respective domain and vice versa, i.e., in a setup with several domains of different spiral chirality, these regions with smaller spiral amplitudes shrink for the benefit of those with larger amplitudes.

A. Intrinsic axial net flow

As shown in [21], global spirals, i.e., a domain of one single spiral type, generate an intrinsic axial net flow that is driven by Reynolds stresses. It is directed oppositely to the phase velocity of the spiral (cf. Sec. V). This intrinsic flow depends on the amplitudes of the SPI velocity field, i.e., smaller amplitudes drive smaller net flow [21]. Thus, in a setup with a separated R- and L-SPI domain with different local amplitudes, the two resulting net flows at the location of the defect do not compensate each other. This difference leads to an axial advection of the defect. In contrast to rigid axial ends, in the periodic boundary case, a global $\langle w(r,\varphi,z)\rangle_{r,\varphi}$ mode is possible and leads to a defect propagation because they behave like impermeable walls (cf. Sec. V) which, however, are blown away like sails in the wind.

Generally speaking, two effects influence the defect behavior in a long system with (several) spiral domains: those with smaller (larger) spiral amplitudes shrink (enlarge) whereas simultaneously producing weaker (stronger) intrinsic axial net flows. Due to the continuity constraint, different intrinsic axial net flows lead to a global axial net flow blowing the defects with different velocities through the system.

If there would be a balance between the local amplitudes, the local intrinsic flows and the global axial flow, then the defect state would be stationary in an axially comoving frame. In our simulations, we could observe such "fragile" states. This changes if one externally imposes an additional axial through flow.

B. External axial through flow and transients

Imposing an external axial through flow Re influences the amplitudes within both spiral domains in different ways. As described in [21] for the global spiral case, the amplitude of the L-SPI (R-SPI) becomes larger (smaller) for positive Re. Therefore, positive Re enlarges the spiral amplitude in the L-SPI domain and reduces the amplitude in the R-SPI domain. The latter then decays and finally disappears when both defects mutually annihilate. This is illustrated in Fig. 6(b) for a P_+/P_- state in a system with Re=4 which disappears for the benefit of a global L-SPI. In order to completely destroy this P_+/P_- state, a minimal Re≈ 1 is needed which depends on the other control parameters.

Furthermore, if Re is switched off instantaneously, the different intrinsic axial flows that is caused by different local spiral amplitudes in the respective spiral domains generate a resulting, nonvanishing global net flow which is directed *oppositely* to the formerly imposed through flow and therefore blows the defects in the *opposite* direction. This can be observed in Fig. 6(a) for Re=2 during the first 1.7 diffusion times and for Re=0 afterwards. The intrinsic driven propagation velocities of the defects are constant and unequal due to the different amplitudes within the R-SPI and L-SPI domains. Once, the amplitudes have become different in size (e.g., by infinitesimal disturbances), the domain with the smaller amplitude shrinks henceforth but does in general not disappear completely.

V. MODE INTERACTION

A global spiral, say an L-SPI can be characterized by its critical amplitudes $u_L := u_{1,1}$, $u_L^\star = u_{-1,-1}$, $w_L := w_{1,1}$, and $w_L^\star = w_{-1,-1}$ (cf. Eq. (4)). The contributions to the $w_{0,0}$ amplitude that is generated by the nonlinear terms uw and w^2 in the w equation of the NSE (Eq. (2)) is given by a combination of these critical modes leading to $u_L w_L + u_L^\star w_L + u_L w_L^\star + u_L^\star w_L^\star$ and $2 w_L w_L^\star$, respectively. Thus, in a global spiral, the NSE allow a nonvanishing, Reynolds stress driven axial net flow $w_{0,0}$ as discussed for example in [21].

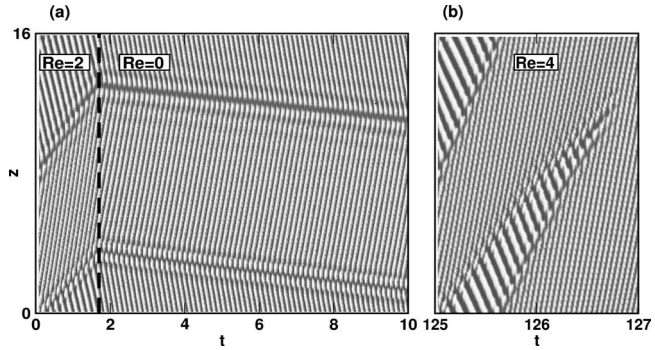

FIG. 6. Numerically calculated spatiotemporal behavior of a $P_{+,\pi}$ and a $P_{-,\pi}$ pair under periodic boundary conditions. (a) $t<1.7$: a nonvanishing axial through flow of Re=2 is applied and the defects propagate downstream with the wind. After switching off the through flow (Re=0) at $t=1.7$ (indicated by the vertical dashed line), the defects propagate in the opposite direction. In (b) the increase in the R-SPI domain at the cost of the L-SPI domain for constant Re=4 is illustrated. Both defects, P_+ and P_-, mutually annihilate ($R_1=140$).

On the other hand, the four critical amplitudes for L-SPI and R-SPI, u_L, $u_L^\star$, $u_R := u_{1,-1}$, and $u_R^\star = u_{-1,1}$ (and the analogous amplitudes for w) combine to $u_L w_L^\star + u_R w_R^\star + u_L^\star w_L + u_R^\star w_R$ via the uw term and to $2(w_L^2 + w_R^2)$ via the w^2 term into the $w_{0,0}$ amplitude.

Considering the substitutions $u_L := u_R e^{2i\alpha}$ and $w_L := -w_R e^{2i\alpha}$ which describes the symmetry transformation $z \to -z$ with an additional phase shift α at the defect (glide-mirror symmetry), one gets $w_{0,0} \equiv 0$ only for $\alpha=\pi$ or $\alpha=0$. In other words, $P_\pm$ defects behave such as impermeable walls between adjacent spiral domains with phase shifts 0 or π. However, further away from the defect, where L-SPI and R-SPI amplitudes are different, there are indeed mirror symmetric, globally circulating closed mean flows on both sides of the defect (Fig. 4).

The $u_{0,0}$ amplitude in the mode spectrum of the radial velocity field u is prohibited by continuity and the radial boundary conditions. Further, the four critical modes u_L, $u_L^\star$, u_R, and $u_R^\star$ combine to $2u_L u_L^\star + 2u_R u_R^\star$ via the u^2 term which vanishes under the same substitutions mentioned above.

At the critical point k_c, ω_c and with the abbreviation

$$(m,n) := f_{m,n} e^{i(m\varphi + nkz)}, \quad f \in \{u,v,w,p\},$$

the two critical spiral modes (1,1) for L-SPI and (1,−1) for R-SPI and their complex conjugates nonlinearly drive (in the vicinity of a $P_\pm$ defect) modes of the form $(0,2)=(1,1)+(-1,1)$ corresponding to axial variations with $2k_c$. The amplitude of the azimuthal $m=0$ mode of our numerically obtained u indeed varies in the defect region with a local axial wave number of about $2k_c$. Additionally, we checked for sev-

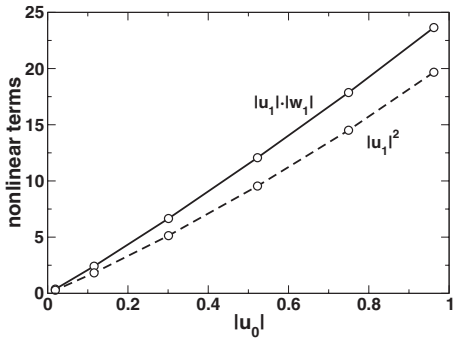

FIG. 7. Mode amplitudes $|u_1||w_1|$ and $|u_1|^2$ versus u_0 [cf. Eq. (3)]. The symbols (○) denote numerically determined values. Lines are interpolations.

eral R_1 that the amplitude of $u_{0,2}$ and similarly that of $w_{0,2}$ in the defect varies *proportional* to the quadratic terms uw and u^2 in the NSE as shown in Fig. 7.

The critical linear instability threshold of CCF against growth of TVF with $m=0$, and $k_{\mathrm{TVF},c} \simeq 4.95$ lies at $R_{1,c} \simeq 118.6$. We observed in the defect region between the spirals an $m=0$ vortex flow with local axial wave number of $k_{m=0} \simeq 7.3$ and furthermore, $k_{\mathrm{SPI}}=3.65$. Thus indeed, near the defect, $k_{m=0} \simeq 2k_{\mathrm{SPI}}$ is unrelated to $k_{\mathrm{TVF},c}$.

VI. APPEARANCE OF THE DEFECTS

A. Defects without axial through flow

Also without an externally imposed axial through flow, P_+ defects arise in a finite system as shown in Fig. 8 which

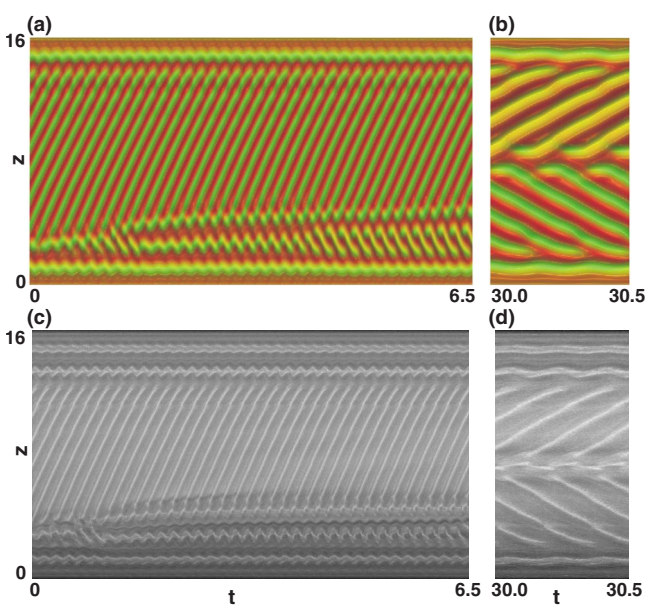

FIG. 8. (Color online) Spatiotemporal behavior of a P_+ defect propagating into a global L-SPI: (a) and (b) color coded numerically simulated radial velocity field $u(z,t)$ at midgap, (c) and (d) flow visualization in experiment. In (a) and (c) the appearance of the defect near the lower lid and its upward propagation is visible. In (b) and (d) a temporal cutout of the final state including the P_+ defect is depicted, the phase shift $\alpha=\pi$ is obvious ($R_1=140$).

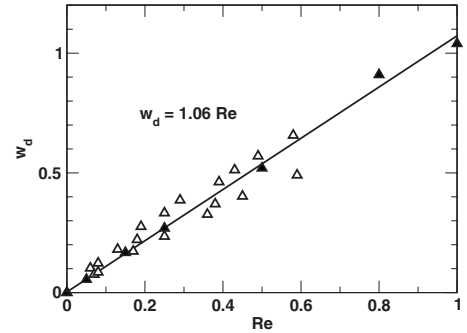

FIG. 9. Experimentally (△) and numerically (▲) obtained axial propagation velocity w_d (measured at midheight) of a $P_{+,\pi}$ defect versus Re. The symbols describe the velocity at midheight for $R_1=140$ and $R_2=-125$. The line is a linear fit.

compares numerically (a), (b), and experimentally (c) and (d) obtained results. It elucidates the spatiotemporal behavior of a P_+ defect in a $\Gamma=16$ system in the absence of an axial through flow.

Starting at $t=0$ with an L-SPI in the bulk, a P_+ defect occurs at the lower Ekman-spiral defect and separates from it. This Ekman-spiral defect thereby changes its behavior from phase generating to annihilating. The P_+ defect propagates toward midheight and after 30 diffusion times, the stationary final state in Fig. 1(a) is accomplished with a phase shift of $\alpha=\pi$. A temporal cutout of this final state including the P_+ defect at midheight and the phase annihilating Ekman-spiral defects at the end walls is depicted in Figs. 8(b) and 8(d). Note, that the axial extension of the spiral in the bulk or, equivalently, the extensions of the Ekman systems near the lids depend on the initial conditions. This holds for simulations as well as for experiments. So, the difference between the here presented numerical and experimental results is not surprising.

B. Defects with axial through flow

Imposing an external axial through flow breaks the symmetry degeneracy of the two SPI solutions. Hence, the Hopf bifurcation to spirals splits up into a branch of downstream propagating L-SPI which bifurcates first and into a branch of upstream propagating R-SPI which bifurcates at a larger R_1. Furthermore, the phase velocities of both spirals are changed [21,22].

We start with the P_+ state [as depicted in Fig. 1(a)], where the P_+ defect is located at midheight of a system with rigid lids, and switch on an axial through flow instantaneously. Then, the P_+ defect begins to propagate downstream. Thereby, the R-SPI domain expands. The *initial* propagation velocity w_d (measured at midheight) of this defect is illustrated in Fig. 9 showing experimental (△) and numerical (▲) results. As expected, the axial propagation velocity w_d is proportional to Re, i.e., to the mean axial flow. In the vicinity of a P_+ defect in an axially comoving frame (velocity w_d), all Fourier modes $|u_m|$ are found to be constant in time.

Numerical and experimental observations showed that the velocity w_d decreases when the defect approaches an axial end wall and, for small through flow ($\mathrm{Re}<0.2$), it stops at a

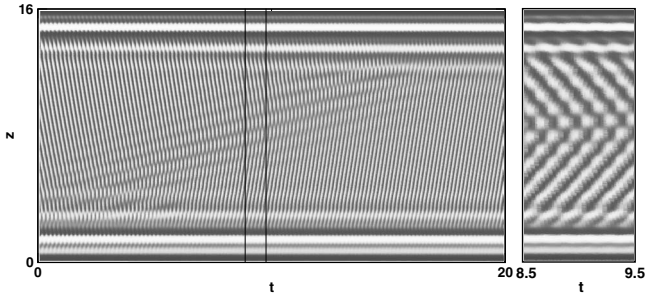

FIG. 10. Spatiotemporal plot of the numerically obtained u field of a $P_{-,\pi}$ defect which mediates the transition from a global R-SPI to a global L-SPI (left). The cutout (right) covers one diffusion time for a better visualization of the defect and the phase shift $\alpha=\pi$. Parameters are $R_1=118$ and Re=0.3.

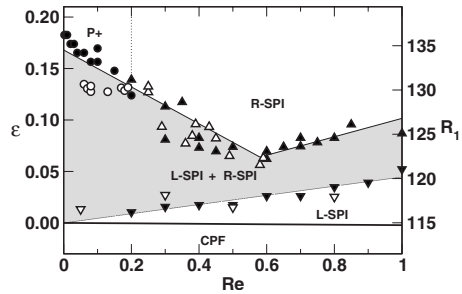

FIG. 11. Phase diagram of CPF, L-SPI, R-SPI, and P_+ states. Open (closed) symbols denote experimental (numerical) results. Stability regions are separated by thin lines to guide the eyes. Upward (downward) oriented triangles identify transitions from global L-SPI to global R-SPI (R-SPI to L-SPI), circles a transition from global L-SPI or R-SPI to stable P_+ states. The vertical dotted thin line roughly indicates a boundary between P_+ states and global R-SPI. The bottom solid, nearly horizontal line represents the bifurcation threshold for SPI. In the range of Re shown here, the thresholds for both spiral types fall together for the given resolution. $\epsilon=R_1/R_{1,c}-1$ with $R_{1,c}=115$ ($R_{1,c}=117.2$) in experiment (numerical calculations). The R_1 axis is based on the experimental $R_{1,c}$.

certain axial position inside the bulk, since the stationary Ekman structure becomes more dominant near the lids. Larger through flow values (Re$>$0.2) are necessary to blow away the defect out of the bulk. In our case of a P_+ defect, the final structure would be a global R-SPI including a phase generating (annihilating) Ekman-spiral defect at top (bottom).

Besides P_+ defects, Fig. 10 displays an example for the generation of a P_- defect with phase shift $\alpha=\pi$ which accrues near the lower lid. An initially existing R-SPI is completely replaced by an L-SPI due to the finite through flow Re=0.3 which blows the $P_{-,\pi}$ defect and the R-SPI out of the bulk. Note that the defect region is wider than that of P_+ states and covers a relatively large area where R-SPI and L-SPI interact to a mixed state.

C. Stability

The numerically determined bifurcation thresholds of L-SPI and R-SPI for periodic boundary conditions are marked as a single thick line in Fig. 11. For positive Re, the bifurcation as well as the absolute instability threshold for R-SPI lie slightly above those of L-SPI but are not distinguishable from them with the resolution in this figure [22,23].

Only stable states are depicted in the phase diagram of Fig. 11; open (closed) symbols refer to experimental (numerical) results. Stability boundaries were mostly determined by varying R_1 quasistatically at fixed Re, starting either from CCF for Re=0 or from Couette-Poiseuille flow (CPF) for Re$>$0. However, also selected Re scans at fixed R_1 have been done. For control parameters in the shaded region, global L-SPI and R-SPI are bistable. The global R-SPI looses stability below the line marked by (∇,$\blacktriangledown$) and undergoes a transition to the global L-SPI via a P_- defect. Hence, for small R_1, the system prefers that spiral type which is traveling *downstream* as in axially periodic systems [21]. On the other hand, above the line marked by ($\triangle$,$\blacktriangle$), the global L-SPI undergoes a transition to a global R-SPI (for Re$\gtrsim$0.2). In both cases the chirality of the spirals is changed via a transient in which a P_+ (L-SPI to R-SPI) or a P_- defect (R-SPI to L-SPI) is generated at the lower (upper) Ekman-spiral defect and then propagates downstream (upstream). In fact, the P_+ (P_-) defect always evolves out of the phase generating (annihilating) Ekman-spiral defect, as described above.

For Re=0, both mirror-symmetric global spiral states undergo a transition to a P_+ state with the P_+ defect at midheight when the driving is increased (quasistatically) beyond $\epsilon=0.17$, cf. Fig. 11. This transition occurs when the phase generating Ekman-spiral defect bounding the global L-SPI (R-SPI) at the lower (upper) end emits a P_+ defect that then moves into the center of the system.

VII. CONCLUSION

Our numerical and experimental study revealed the existence of stable defects between oppositely traveling spiral waves in counter-rotating Taylor-Couette flow. Defects either generate (P_+) or annihilate phase (P_-) and separate domains of different spiral chirality with a distinct phase difference of either 0 or π at the domain wall. Thus, four different types, namely $P_{+,0}$, $P_{+,\pi}$, $P_{-,0}$, and $P_{-,\pi}$ can be observed. These defects are stabilized by a nonlinear mode coupling and behave like impermeable walls. This means, that in the spiral domains above and below the defects a large circulation caused by the axisymmetric $m=0$ modes has been observed. Near the inner cylinder in both systems the flow is thereby axially directed to the same direction as the phase propagation of the corresponding spiral (upwards for L-SPI and downwards for R-SPI).

Under periodic boundary conditions, defects always occur as a $P_{+,\pi}/P_{-,\pi}$ pair. Their stability depends on the mean axial flow which may either be externally imposed or a consequence of initially different amplitudes in the R-SPI and L-SPI domain (intrinsic net flow) and stimulates both defects to axially propagate with, in general, different velocities. Thus, the defects approach each other and, for sufficiently strong Re, mutually annihilate. For moderate or vanishing

through flow, on the other hand, we observed stable P_+/P_- configurations.

In the finite system, a single defect travels, due to the Ekman profile, toward the axial middle of the bulk and the final P_+ or P state is stable. However, small externally imposed axial through flow influences the defect propagation and changes its final axial position. For stronger through flow, a transition scenario from a global R-SPI state to a global L-SPI state or vice versa is mediated by a propagating defect pushing one spiral domain out and pulling the other through the bulk.

ACKNOWLEDGMENTS

We acknowledge support from the Deutsche Forschungsgemeinschaft. G.P., M.H., and J.A. thank K. Hochstrate for assistance during some experimental measurements.

[1] A. Joets and R. Ribotta, J. Stat. Phys. **64**, 981 (1991).
[2] E. Bodenschatz, W. Pesch, and G. Ahlers, Annu. Rev. Fluid Mech. **32**, 709 (2000).
[3] M. C. Cross and P. C. Hohenberg, Rev. Mod. Phys. **65**, 851 (1993).
[4] P. Habdas, M. J. Case, and J. R. de Bruyn, Phys. Rev. E **63**, 066305 (2001).
[5] L. Pastur, M.-T. Westra, D. Snouck, W. van de Water, M. van Hecke, C. Storm, and W. van Saarloos, Phys. Rev. E **67**, 036305 (2003).
[6] A. Ezersky, N. Latrache, O. Crumeyrolle, and I. Mutabazi, Theor. Comput. Fluid Dyn. **18**, 85 (2004).
[7] P. Coullet, T. Frisch, and F. Plaza, Physica D **62**, 75 (1993).
[8] M. van Hecke, C. Strom, and W. van Saarloos, Physica D **134**, 1 (1999).
[9] A. Newell, T. Passot, and J. Lega, Annu. Rev. Fluid Mech. **25**, 399 (1993).
[10] C. M. Aegerter and C. M. Surko, Phys. Rev. E **63**, 046301 (2001).
[11] I. S. Aranson and L. Kramer, Rev. Mod. Phys. **74**, 99 (2002).
[12] S. Madruga, H. Riecke, and W. Pesch, Phys. Rev. Lett. **96**, 074501 (2006).
[13] R. Tagg, Nonlinear Sci. Today **4**, 2 (1994).
[14] P. Chossat and G. Iooss, *The Couette-Taylor Problem* (Springer, New York, 1994).
[15] C. Hoffmann, M. Lücke, and A. Pinter, Phys. Rev. E **72**, 056311 (2005).
[16] M. Heise, D. Küter, J. Abshagen, and G. Pfister, J. Phys.: Conf. Ser. **137**, 012004 (2008).
[17] D. Coles, J. Fluid Mech. **21**, 385 (1965).
[18] C. D. Andereck, S. S. Lui, and H. L. Swinney, J. Fluid Mech. **164**, 155 (1986).
[19] W. F. Langford, R. Tagg, E. J. Kostelich, H. L. Swinney, and M. Golubitsky, Phys. Fluids **31**, 776 (1988).
[20] M. Heise, C. Hoffmann, J. Abshagen, A. Pinter, G. Pfister, and M. Lücke, Phys. Rev. Lett. **100**, 064501 (2008).
[21] C. Hoffmann, M. Lücke, and A. Pinter, Phys. Rev. E **69**, 056309 (2004).
[22] J. Abshagen, M. Heise, J. Langenberg, and G. Pfister, Phys. Rev. E **75**, 016309 (2007).
[23] A. Pinter, M. Lücke, and C. Hoffmann, Phys. Rev. E **67**, 026318 (2003).